Podeur and Vogt *EPJ Techniques and Instrumentation* (2022) 9:6
https://doi.org/10.1140/epjti/s40485-022-00082-1

EPJ Techniques and Instrumentation

RESEARCH ARTICLE Open Access

Experimental evaluation of heat transfer effect on turbocompressor performance operating with helium-neon gas mixtures

Maxime Podeur[1*] and Damian M. Vogt[1]

*Correspondence:
maxime.podeur@itsm.uni-stuttgart.de
[1]Institute of Turbomachinery and Machinery Laboratory, University of Stuttgart, Stuttgart, Germany

Abstract

Within the framework of the Future Circular Collider (FCC) currently being investigated at CERN, the entire cryogenic cycle had to be revised with respect to the existing Large Hadron Collider (LHC). In particular, a novel pre-cooling cycle had to be developed for this purpose. This led to a closed-loop cryogenic cycle operating with a mixture of helium and neon, also called Nelium. To better understand the challenges and opportunities associated with the design and operation of radial compressors with such light gases, a closed loop test facility has been designed, built and commissioned at the ITSM (University of Stuttgart). The test facility has been developed to operate with air as well as with helium-neon gas mixtures of varying mixing ratios ranging from pure neon to pure helium. In this paper, the test facility architecture and operation procedure are briefly introduced together with a description of the newly installed compressor stage. Experimental performance measurements are then compared to adiabatic and diabatic numerical simulation validating respectively the pressure rise and diabatic stage efficiency for various gases. The heat transfer effect on compressor stage performance is then described and the respective contribution of the influencing factors are quantified.

Keywords: Turbocompressor; Light gases; Diabatic compression

1 Introduction

With CERN's FCC project [1] designed with a three times longer perimeter ring and equipped with superconducting magnets featuring twice larger magnetic fields than the LHC, a substantial increase in heat load required a fundamental review of the cryogenic cycle architecture. A closed loop pre-cooling cycle is now foreseen to pre-cool the main helium cryogenic cycle as well as to maintain key components in the 40 to 60 K range. In comparison to the LHC [2], this more sustainable pre-cooling cycle avoids the need for an additional storage of LN2 and allows for a thermodynamically more efficient repartition of heat loads. Additionally, with the objective of developing an overall efficient cryogenic cycle, research is currently being conducted to investigate the implication of replacing the standard screw compressor used in conventional cryogenic cycle by turbocompressor technology yielding a greater efficiency. To make this change economically viable and facil-

itate the compressor pressure rise, helium is ballasted with a heavier gas that is neon. The molecular weight of this gas mixture remaining particularly low, such a decision implies a compressor operating range rarely encountered in most turbocompressor applications [3, 4]. In fact, while the compressor stage is forced to remain in a low range of characteristic rotational speed due to the high gas speed of sound, an ulta-high-speed compressor is required to reach the desired pressure rise. In order to validate the performance of such compressor tailored for light gas application, a novel test facility has been designed and recently commissioned at the University of Stuttgart. The latter features an ultra-high-speed turbocompressor directly driven by a permanently cooled motor. However, due to the presence of a coolant flowing inside the motor housing a heat transfer occurs with the operating gas leading to the impossibility of acquiring an accurate measurement of the stage adiabatic efficiency. A similar problem can be found in other applications such as fuel cell compressor or turbocharger, where the coolant is replaced by a heat source due to the presence of a hot gas entering the turbine [5, 6]. In a more general manner, turbomachines of a relatively small size and thus low power can be subject to these uncertainties. This issue is accentuated in our specific application due to the inherent low compressor power for light gas operation. All these applications justify the need for a better understanding of this heat transfer effect and in turn the search for a reliable model to retrieve adiabatic compressor performance from experimental diabatic performance. The following paper attempts at characterising and quantifying the heat transfer effect on compressor stage performance using both experimental measurement and numerical simulation. To that end, the test facility is first presented including its operating procedure as well as a description of the objective behind the measurement campaign. Emphasis is then brought on the compressor stage with the presentation of the stage geometry and the set-up of numerical simulations. Results are then presented starting with the adiabatic performance validation. The heat transfer effect on stage performance is then described combining experimental measurements and results of Conjugate Heat Transfer (CHT) simulation. Finally, the respective contribution of potential influencing factors on the heat transfer rate are quantified.

2 Theoretical background on turbocompressor performance

A turbocompressor can be defined as a device in which energy is transferred from a rotating element to a fluid flowing continuously. In the perspective of later comparing the aerodynamic performance of turbocompressor between experimental and numerical prediction, a summary of key parameters and governing relations is presented here below. The compressor performance commonly characterised by its pressure ratio π and efficiency η_p can be defined by expression (1) such that both parameters are a function of the stage geometry characterized by the impeller diameter D_2 and impeller outlet width h_2, the mass flow rate $\dot{m}$, the rotational speed Ω and boundary conditions such as the inlet pressure P_1, inlet temperature T_1 or gas properties including the specific heat capacity at constant pressure and gas constant respectively c_p and r.

$$\pi, \eta_p = f(D_2, h_2, \dot{m}, \Omega, P_1, T_1, c_p, r, \ldots), \tag{1}$$

where subscript 1 refers to the inlet stage measurement plane and subscript 2 refers to the rotor outlet when associated to geometrical parameter and to the stage outlet plane

when associated to thermodynamic parameters. As in many engineering fields, a similitude analysis is often employed to develop similarity conditions and is detrimental here to quantify and characterise compressor performance with varying operating condition, boundary condition or scale. Thus, following the traditional Buckingham-Π theorem, a new set of non-dimensionalised parameters can be derived to define compressor performance as follows:

$$\eta_p, \psi_p = f(\phi_{t1}, M_{U2}, \mathrm{Re}, h_2/D_2, \gamma), \tag{2}$$

where a ratio of impeller characteristic length h_2/D_2 quantifies the geometrical similitude. The total inlet flow coefficient ϕ_{t1} and a characteristic Reynolds number Re are used to determine the fluid dynamic similitude, which are respectively defined as:

$$\phi_{t1} = \frac{\dot{m}}{\rho_{t1} D_2^2 U_2}, \tag{3}$$

$$\mathrm{Re} = \frac{U_2 D_2}{\nu}, \tag{4}$$

where U_2 is the impeller tip speed defined as $U_2 = \pi/60 \Omega D_2$, ρ_{t1} is the total inlet gas density defined as $\rho_{t1} = P_1/rT_1$ and ν is the gas kinematic viscosity.

Finally, thermodynamic similitude is defined using the specific heat ratio γ as well as the tip Mach number M_{U2} defined as:

$$M_{U2} = \frac{U_2}{\sqrt{\gamma r T_1}}. \tag{5}$$

Then, the primary parameters commonly used in the characterization of turbocompressor performance are the pressure ratio π and the polytropic efficiency η_p defined as:

$$\pi = \frac{P_2}{P_1} = \left[1 + (\gamma - 1)\lambda M_{U2}\right]^{\frac{\eta_p \gamma}{\gamma - 1}}, \tag{6}$$

$$\frac{P_2}{P_1} = \left(\frac{T_2}{T_1}\right)^{\frac{\eta_p \gamma}{\gamma - 1}}. \tag{7}$$

Additional parameters characterising compressor performance such as the work input λ, the pressure coefficient ψ_p and the reduced mass flow rate $\dot{m}_{\mathrm{red}}$ are particularly well suited for the comparison of compressor performance operating with different gases as it is the case in this specific study. These parameters extensively used in the result section are defined as:

$$\lambda = \frac{c_p(T_2 - T_1)}{U_2^2}, \tag{8}$$

$$\psi_p = \lambda \eta_p, \tag{9}$$

$$\dot{m}_{\mathrm{red}} = \phi_{t1} M_{U2} \sqrt{\gamma}. \tag{10}$$

To conclude on the fundamentals of turbocompressor performance, Fig. 1 provides a typical performance curve illustrating the off-design operation behaviour at a specific rotational speed.

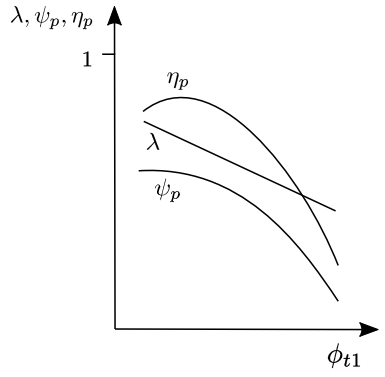

Figure 1 Off-design performance of turbocompressor

3 Presentation of the Nelium turbocompressor test facility

3.1 Test facility architecture and apparatus

As part of a cooperative research project between CERN, TU Dresden, University of Stuttgart and MAN Energy Solutions on the advantage and challenges associated to the operation of turbocompressor with light gases, a novel test facility has been recently commissioned at the University of Stuttgart. A picture of the latter with the key components is shown on Fig. 2 and the associated P&ID is provided in Fig. 3.

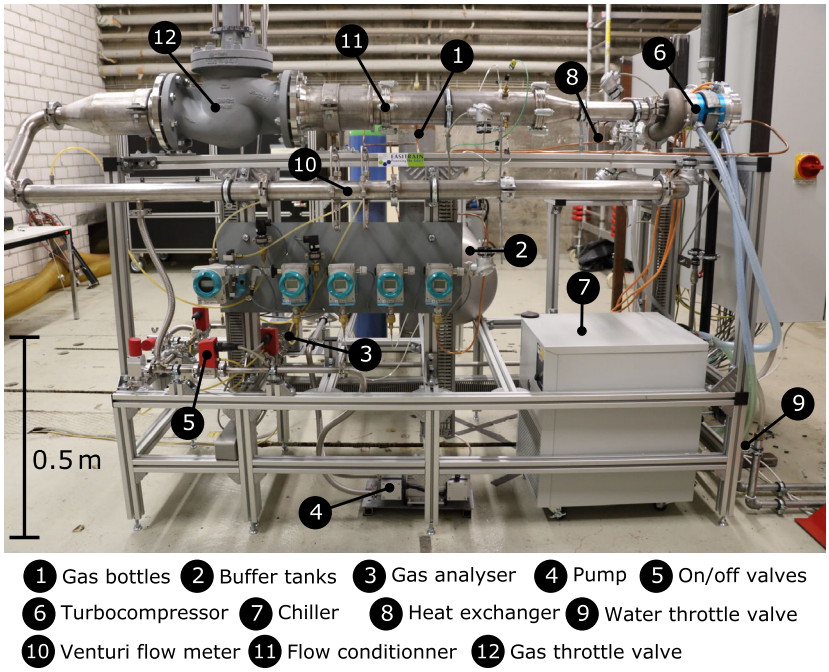

Figure 2 Picture of the Nelium turbocompressor test facility (ITSM - University of Stuttgart)

Its primary objective is to acquire and compare the steady state compressor stage performance for a wide variety of low molecular weight gases. To satisfy this goal, a low vacuum tightness as well as a resistance to helium leakage is required and justifies the choice of components and fittings commonly found in cryogenic application rather than in the tur-

bomachinery field. As shown on this picture, the test facility is comprised of a first section (label numbers 1 to 5) where buffer tanks are pressurised with either a pure gas such as helium and neon or any binary gas mixture prepared by partial pressure. The obtained mole fraction is then measured by a binary gas analyser. An air supply is also connected to the test facility so that compressor performance can be measured for gases with a molecular weight ranging from 4 g/mol to 29 g/mol.

Connected to this buffer volume is the closed-loop turbocompressor test section (label numbers 6 to 12). It is first comprised of the compressor itself in which energy is transferred to the fluid by deviating and accelerating the flow into the impeller. The kinematic energy gain is then converted into pressure rise through the diffuser and the volute part of the compressor stage. In addition to this pressure rise, the temperature increases firstly following the isentropic thermodynamic process. In addition, aerodynamic losses are responsible for an entropy increase through the stage leading to an additional temperature increase in order to maintain the same outlet pressure.

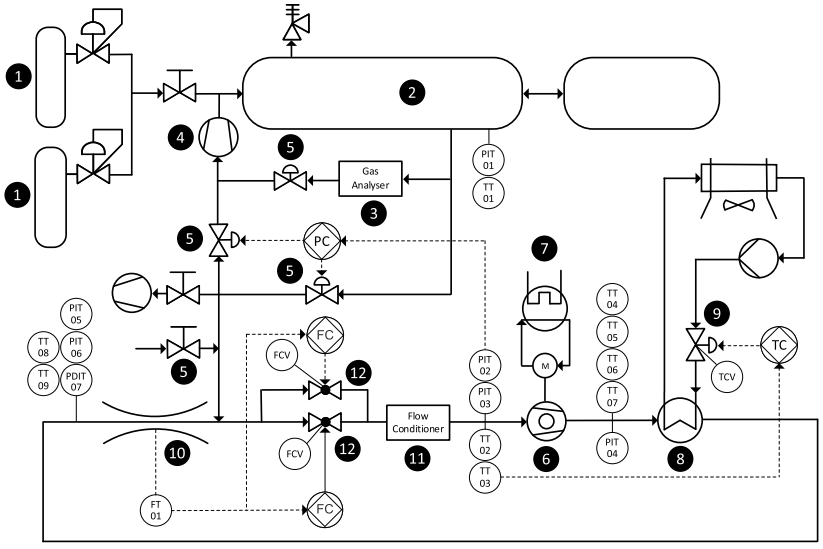

Figure 3 P&ID of the Nelium turbocompressor test facility (ITSM - University of Stuttgart)

A plate heat exchanger is connected downstream of the compressor to offset the enthalpy rise generated by the compressor stage. Flow then passes through a Venturi flow meter, allowing to measure the operating mass flow rate. The flow is then throttled with two valves placed in parallel enabling the removal of the pressure rise generated upstream by the compressor. Downstream of these valves, a flow conditioner is placed to remove the flow uniformities before it can re-enter the compressor stage.

To acquire the compressor stage performance, total pressure and temperature probes are located upstream of the stage and static pressure taps as well as Resistance Temperature Detectors are positioned downstream of the stage to measure respectively the static outlet pressure and temperature. Additional pressure and temperature sensors are attached to the Venturi flow meter designed following the ISO 5167-4 norm in order to evaluate the operating mass flow rate. All sensors are calibrated in-situ including the whole

measurement chain. A Data Acquisition System (DAS) retrieves the measured parameters which are post processed with a moving average and the calculation of relative standard deviation. All measured data and calculated performance parameters are then displayed on the Human Machine Interface (HMI) in real time. In addition to the DAS, a Programmable Logic Controller (PLC) retrieves parameters required to insure a safe operation of the test facility. Feedback positioning of the actuators are thus monitored by the PLC and in turns control their position to satisfy both the user request and a compressor operation away from aerodynamic instability regions.

In order to maintain a constant inlet pressure while conserving a degree of freedom in the operating mass flow rate, gas can be exchanged between buffer tank and test loop. In practice, the mass flow rate is coarsely set using the largest throttle valve and the position of the small one is then adjusted for the fine tuning. Inlet pressure is programmatically controlled around a target value via the PLC by triggering fast acting on/off valves connected to the buffer tank. The stage inlet temperature is PID controlled through the PLC by adjusting the throttle valve position connected to the cooled water supply.

Additional details on the test rig equipments and operation of the facility can be found in [7]. However, a major difference with the architecture presented in this previous paper is the compressor aerodynamic geometry, which has been substantially changed. An illustration of the new compressor stage including the measurement planes is shown in Fig. 4.

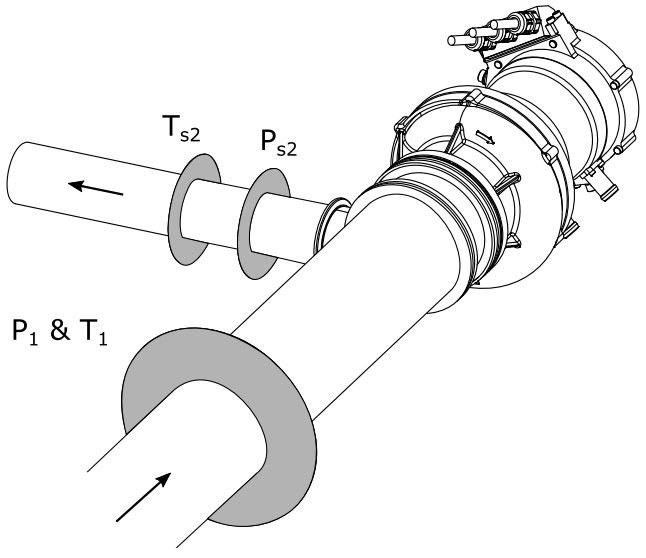

Figure 4 Compressor stage layout and measurements planes

The impeller shaft is rotated with an ultra-high-speed drive supported by gas bearing and designed to reach rotational speed up to 120,000 rpm with a rated aerodynamic power of 15 kW. Finally, to ensure the safe operation of this high power density motor, coolant is pumped from a chiller with consequences on the operating gas temperature presented in the next section.

3.2 Motor coolant and temperature housing instrumentation

As previously mentioned, the motor is maintained at a reasonable operating temperature with a coolant flowing continuously through the motor housing. The coolant first leaves the chiller at a prescribed set temperature, then enters the motor housing before going to the power supply and finally flows back to the chiller. Inside the motor housing, the coolant is responsible for a heat removal from the surrounding walls. As a result, the heat generated by the hot operating gas is convected away by forced convection. This leads to a diabatic outlet temperature lower than the theoretical adiabatic one and a measured diabatic efficiency above the adiabatic one.

In order to monitor the temperature distribution resulting from the thermal equilibrium inside the housing body, several type-k thermocouples are positioned on the housing wall after having been calibrated in-situ. The sensor tip is thus maintained in contact with the body surface and thermally insulated from the outside environment. Their position is indicated on Fig. 5(b) together with a picture illustrating the occurring heat transfer on Fig. 5(a).

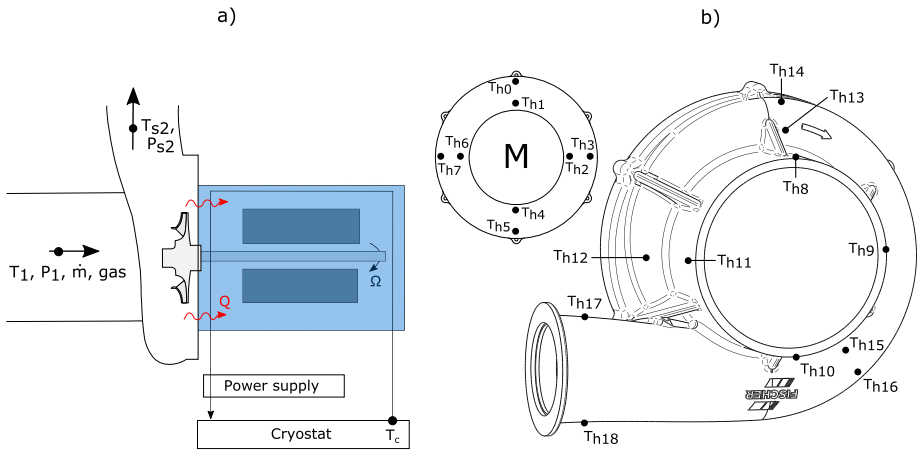

Figure 5 (**a**) Illustration of the occurring heat transfer phenomena and (**b**) positioning of the temperature sensors on the compressor housing

3.3 Uncertainty analysis

Before providing experimental results, the section below summarises the detailed uncertainty analysis presented in [7]. First, Table 1(a) provides the uncertainty in the averaged measured inlet and outlet pressure and temperatures together with the sensors calibrated range. These uncertainties are comprised of the individual uncertainty of sensors after calibration and additional sources of error such as the geometry of pressure taps, the recovery factor of probes, the effect of natural convection or the uncertainty in averaging a thermodynamic quantity with a limited number of sensors. These different uncertainties are combined using the root-sum square method and can vary depending on the operating point, which explains the range of uncertainties for pressure and temperature displayed in Table 1(a). The uncertainty in the measured Nelium mole fraction, compressor rotational speed and gas flow rate is also provided in this same table.

Table 1 Summary of the uncertainty analysis on (a) measured parameters and (b) calculated compressor performance parameters

(a)		
Parameter	Uncertainty FS	Calibrated Range
P_{in}	± 0.03 - 0.05 %	0.8 - 1.2 bar
$P_{s,\text{out}}$	± 0.02 - 0.04 %	0.8 - 1.6 bar
T_{in}	± 0.06 - 0.08 %	30 - 90°C
$T_{s,\text{out}}$	± 0.03 - 0.05 %	30 - 90°C
x_{gas}	± 0.04 %	0 - 1
Ω	± 11 RPM	0 - 120 kRPM
$\dot{Q}$	± 0.23 %	0.4 - 15 m^3/min

(b)	
Parameter	Uncertainty
π	± 6.9e^{-4} [-]
η	± 1.5e^{-2} [-]
M_{U2}	± 1.0e^{-4} [-]
$\dot{m}_{\text{red}}$	± 7.9e^{-4} [-]
λ	± 2.5e^{-3} [-]
ϕ_{t1}	± 1.4e^{-3} [-]
ψ_p	± 1.1e^{-2} [-]

The propagated uncertainty to the calculated compressor performance parameters are then given in Table 1(b) for a specific operating point corresponding to air operation at a tip Mach number M_{U2} of 0.48 and a reduced mass flow rate $\dot{m}_{\text{red}}$ of 0.0404.

3.4 Measurement campaign

The heat transfer depicted above between the operating gas and the housing wall is subject to various possible factors. A first one would be the compressor operating point, namely the mass flow rate and the impeller outlet temperature. Then, the operating gas defined by its density, heat transfer coefficient and specific heat capacity is also suspected to have a major impact. A change in inlet temperature at a specific reduced mass flow and rotational speed would also vary the impeller outlet temperature and with it the heat transfer rate. Finally, the chiller set temperature and with it the coolant temperature inside the motor housing influences the housing external wall temperature and with it the heat transfer rate. The measurement campaign described hereafter attempts at determining their respective contributions. Steady state performance measurements have been conducted with air, neon, helium and a mixture of helium and neon at 50/50 mole fraction, which will be later referred to as Nelium05. Moreover, for each of these gases, the performance map is drawn at three tip Mach number M_{U2} of respectively 0.24, 0.36 and 0.48 except for helium, where a maximum tip Mach number of 0.29 can only be reached due to the maximum motor rotational speed. These performance maps are then acquired for a range of inlet temperature between 15°C and 25°C and a range of chiller temperature between 15°C to 30°C. This measurement campaign was conducted over 32 days and each measured operating point was acquired several times for repeatability purposes.

4 Compressor geometry understudy and numerical set up

The compressor stage presented hereafter is the result of an aero-mechanical design optimisation intended to be used in an industrial high-speed multi-stage machine operating with low molecular weight gases. The result is a shrouded impeller with vaned diffuser. In order to validate experimentally the stage aerodynamic performance, a scaled version of the latter with an impeller diameter of 68.5 mm has been manufactured combining 5-axis machining and Electrical Discharge Machining. On the test facility, the flow enters the stage radially guided by Inlet Guide Vane (IGV) and leaves through a volute as depicted on Fig. 6.

The compressor stage performance has been evaluated numerically by first assuming an adiabatic compression. The whole fluid domain is thus discretised with a single sector structured mesh using Numeca Autogrid 13.1 [8] for respectively the IGV, the impeller,

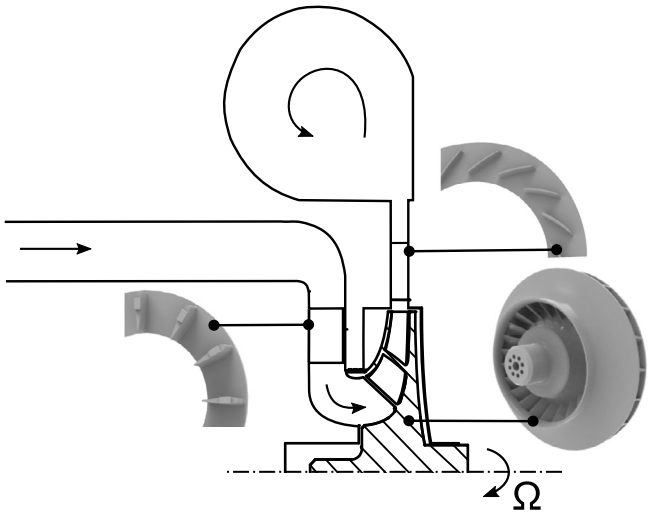

Figure 6 Meridional view of the compressor stage and 3D representation of the IGV, impeller and diffuser

the diffuser and the cavities on the hub and shroud side of the impeller. The volute is then discretised with an unstructured mesh including a refinement near the walls and tongue using ANSYS ICEM CFD [9]. The whole fluid domain amounts to 1,853,495 elements. Mixing planes are set at the different rotor-stator interfaces and no slip boundary conditions are applied on adiabatic walls.

Steady state calculations are conducted with ANSYS CFX 2020.1 [9], where The Reynolds Averaged Navier-Stokes (RANS) equation are closed with the Shear Stress Transport (SST) turbulence model. After a comparison with the most commonly used turbulence models, the SST model recommended as best practice with ANSYS CFX 2020.1 [9], provides the best agreement with experimental results for the setup understudy. Mass flow rates, pressure ratio and stage efficiency are monitored as well as the relative standard deviation, which is used as a convergence criterion. Total inlet pressure and temperature are prescribed at the domain inlet plane. Static pressure is then varied at the outlet plane to generate speedlines comprised of 7 operating points. Finally, operating gases are modelled as ideal with properties provided by REFPROP [10] and mixing laws. Boundary conditions and gases used are identical to the ones chosen for the measurement campaign. To illustrate the flow regime and turbulence level of these Computed Fluid Dynamics (CFD) simulations by taking the example of an operating point in the middle of the air performance map, the characteristic Reynolds number is evaluated to 6.9×10^4 and 7.3×10^5 for respectively the inlet pipe flow and the one characterised by the impeller tip speed and diameter.

On top of these adiabatic simulations, the stage performance has been evaluated using Conjugate Heat Transfer simulation. To that end, the whole housing including the inlet, labyrinth teeth, diffuser blades, volute and plates have been discretised with an unstructured mesh amounting to 925,880 tetrahedral elements. Solid-fluid interfaces have been set between the solid and the fluid domain where forced convection occurs. Wall temperature is monitored at the same location as depicted in Fig. 5.

Material properties are prescribed to the associated bodies, which are made of different aluminium and stainless-steel alloys. O-ring grooves and rubber rings are simulated as

volume with adiabatic walls. Natural convection is prescribed at the housing outer wall. A first heat flux is prescribed at the inlet flange resulting from conduction with a colder inlet piping. A second heat flux is prescribed at the housing rear plate where most of the heat is removed due to the coolant flowing inside the motor housing. Since the exact temperature distribution at this location is unknown, a heat flux is first prescribed so that the evaluation of T_{h1} corresponds to the experimental value. The heat flux at the inlet surfaces is then set so that T_{h8} also matches with experimental value. The diabatic simulation setup with the boundary conditions and interfaces is summarised in Fig. 7.

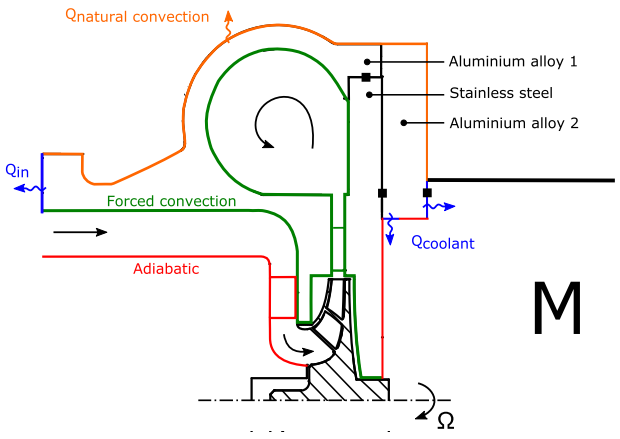

Figure 7 Scheme of the occuring heat transfer along the compressor housing wall and boundary conditions set for the Conjugate Heat Transfer simulation

5 Adiabatic performance validation

As previously introduced, experimental measurements have been conducted for various gases. In this section, results are presented at a fixed inlet temperature of 25°C and a chiller set temperature of 20°C. Firstly, Fig. 8(a) compares the measured pressure ratio for the case of air and neon operation to the numerical prediction with the hypothesis of adiabatic compression.

For the three tip Mach number shown, an overall good agreement for the two gases between the experimental measurements and numerical prediction is observed. For a fixed tip Mach number an upward shift in pressure ratio and mass flow rate due to an increase in specific heat ratio can also be noticed when moving from air to neon operation. This is best explained by analysing equation (6) as well as the reduced mass flow rate definition (10). By assuming a constant work input and efficiency at a specific inlet flow coefficient and tip Mach number, a change in specific heat ratio directly leads to a change in pressure ratio and reduced mass flow rate.

The hypothesis of constant efficiency and work input at a specific inlet flow coefficient would imply a constant pressure coefficient as defined by equation (9). In reality however, changing the gas properties leads to a change in characteristic Reynolds number, which in turns impact the efficiency, pressure coefficient and inlet flow coefficient [11]. This Reynolds number effect is captured by the pressure coefficient measurements shown

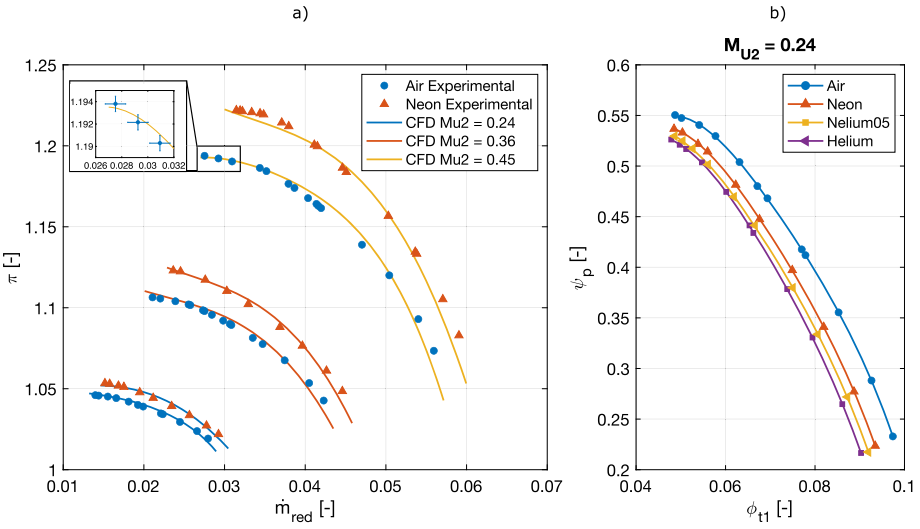

Figure 8 (**a**) Comparison of the experimental and numerical compressor performance map for the case of air and neon operation and (**b**) experimentally acquired pressure coefficient distribution for air, neon, nelium05 and helium operation illustrating the Reynolds number effect

on Fig. 8(b), where the latter increases as the Reynolds number of the respective gases increases.

The measured efficiency is another useful performance parameter to observe the Reynolds number effect. However, due to the heat transfer effect mainly caused by the presence of the coolant inside the motor housing, the measured diabatic efficiency does not follow the adiabatic numerical prediction as it will be presented in the next section. Finally, the good agreement for the pressure ratio between experimental measurements and numerical prediction suggest that the pressure rise is not affected by the heat transfer as it will be later confirmed experimentally.

6 Experimental heat transfer effect analysis and numerical validation

Before analysing the heat transfer effect on the overall stage performance, and in particular its efficiency, Fig. 9(a) provides an illustration of the temperature distribution on the compressor housing as well as the gas temperature in one volute section (b)).

These numerical diabatic results are obtained for neon operation at a tip Mach number of 0.36 and an inlet flow coefficient of 0.07. It first shows how heat is convected from the hot operating gas towards the housing wall temperature. Heat is then transferred by conduction towards the front and the back of the compressor where heat is removed. In this specific case, 84%, 14.4% and 1.6% of the total cooling power is attributed to respectively the heat flux prescribe on the housing back plate, the one on the inlet housing surface and the forced convection applied on the housing outer surface. A temperature gradient normal to the housing surface and resulting from the prescription of non-adiabatic walls can be observed on Fig. 9(b). The force convection acting on the whole housing surface is thus responsible for a reduction of the gas temperature and in turns a measured diabatic efficiency above the theoretical adiabatic one.

Similar to numerical results presented on Fig. 9, additional diabatic simulations have been conducted as previously described. Figure 10(a) compares the housing wall tem-

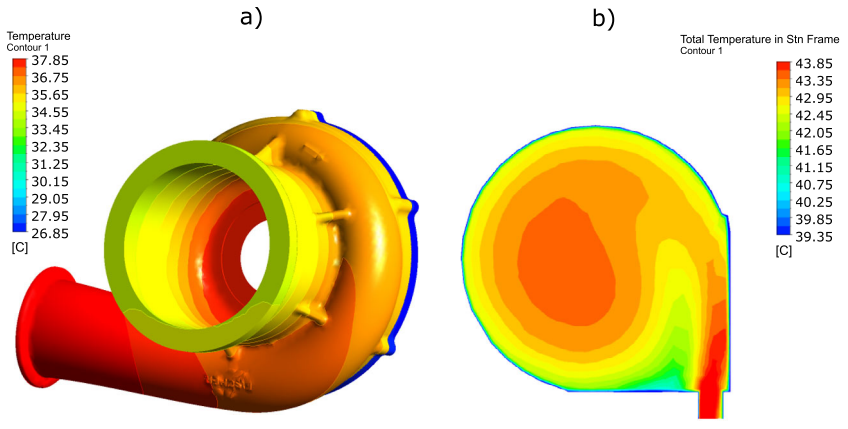

Figure 9 (**a**) Housing wall temperature distribution and (**b**) hot gas temperature distribution on a volute section resulting from CHT simulation

perature measured at five operating points to numerical predictions. Overall, the measured temperature distribution on the housing outer wall is well captured by the numerical prediction. The first three operating points correspond to air operation at three tip Mach number and about the same inlet flow coefficient of 0.07. With increasing tip Mach number the impeller outlet temperature progressively increases together with the motor power. In turns, the thermal equilibrium leads to an increase of the housing outer wall temperature. The last two operating points correspond to neon operation. All temperatures at a same tip Mach number than for air operation are thus higher due to a higher specific heat ratio and a resulting higher impeller outlet temperature.

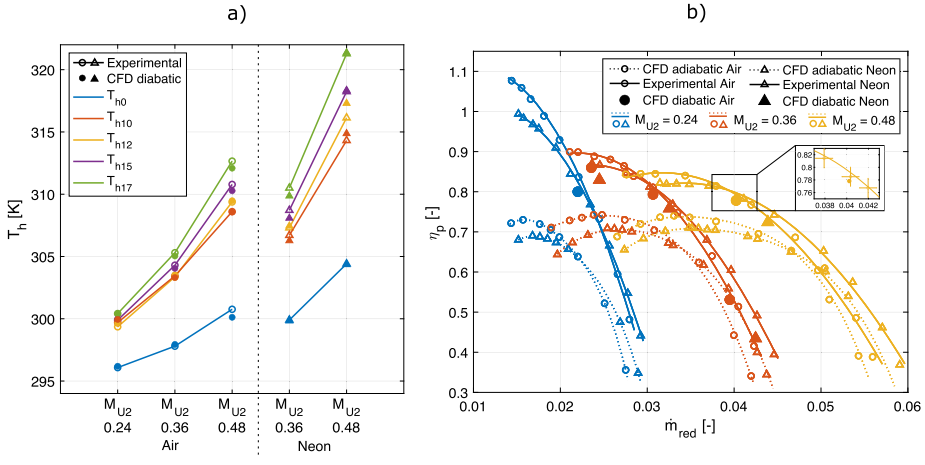

Figure 10 (**a**) Comparison of experimental housing wall temperatures to numerical predictions at five operating points and (**b**) Comparison of measured adiabatic stage performance to the numerically predicted adiabatic and diabatic one for air and neon operation

In addition to these operating points, identical simulations have been conducted at different inlet flow coefficient closer to surge and choke operation and the resulting stage performance are compared to numerical results on Fig. 10(b). Numerically predicted adi-

abatic efficiency for the same tip Mach number are also provided as a reference. Some observation can be first drawn by comparing predicted adiabatic efficiency to measured diabatic ones. It can thus be noticed that at a fixed rotational speed, the difference in efficiency tend to decrease as the mass flow rate increases. Indeed, with an increase in hot gas flow, heat removal becomes more and more difficult for an almost constant cold source temperature. Then, the difference in efficiency also tends to decrease as the rotational speed increases. In fact, even if the temperature difference between hot gas and cold wall increases as well as the Reynolds number and with it the heat transfer coefficient, the stage temperature difference increases more rapidly than the outlet temperature reduces by heat transfer. This results in a measured efficiency decreasing towards the adiabatic numerical prediction as the tip Mach number increases.

Concerning the comparison between measured diabatic efficiency and numerical prediction, a good agreement is obtained for operating points at intermediate mass flow rate at the three rotational speeds and for the two gases. At lower and higher mass flow rate, even if most of the efficiency difference with the adiabatic case is captured by the CHT simulations, larger differences are observed with experimental measurements. In depth investigation would be required to determine the source of these differences but possible reason include the surface roughness effect which is known to play a major role on forced convection. Additionally, mixing planes at rotor-stator interfaces also smoothen the azimuthal temperature gradient propagated downstream.

Previous observations have been made for a constant inlet temperature T_1 and chiller set temperature T_c. Varying the chiller set temperature leads to a change in cold source temperature and in the heat removed from the housing wall and operating gas. Figure 11 shows the experimental stage performance at a constant tip Mach number of 0.36 for neon operation at four different chiller set temperature. Numerical adiabatic predictions are also provided as a reference.

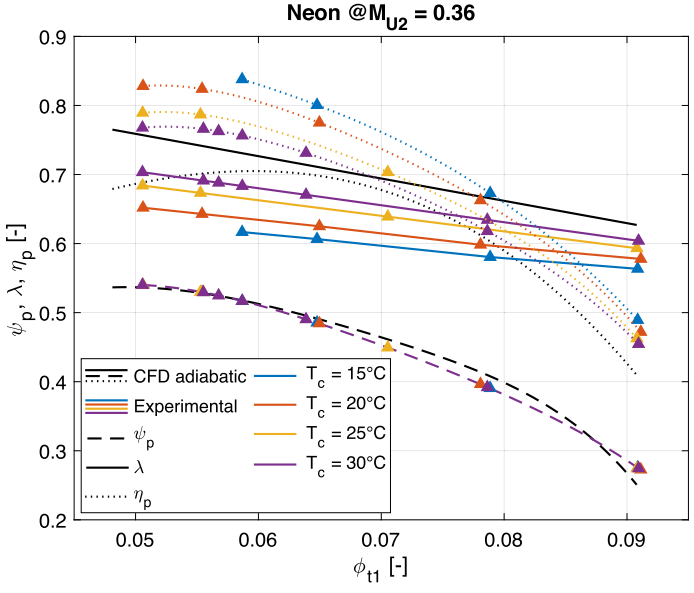

Figure 11 Experimental diabatic compressor stage performance for the case of neon operation at a tip Mach number of 0.36 and at four chiller set temperature together with the adiabatic numerical prediction

Starting with pressure coefficient, the overlay of measurement points on a same distribution confirms the affirmation made previously that the pressure rise is not affected by the heat transfer. Furthermore, it illustrates the good repeatability of the experiment conducted over different days.

On the other hand, the efficiency and work input displayed on this same figure are heavily impacted by a change in chiller set temperature. It can be observed that as the chiller temperature increases, the heat transfer with the operating gas reduces and the measured efficiency decreases towards the numerically predicted adiabatic efficiency. In parallel, the work input increases for a fixed inlet flow coefficient and the slope of the latter in absolute value increases as well.

In order to conclude this heat transfer effect analysis, the inlet flow coefficient, tip Mach number, inlet temperature, chiller set temperature and operating gas properties have been varied individually to characterise their respective impact on the measured performance. To that end, a reference work input distribution is taken by choosing the numerically predicted one in the case of adiabatic compression, which is a reasonable assumption for a low tip Mach number range of operation as it is the case for light gas application. Hence, the difference between the measured diabatic work input $\lambda_{d,\mathrm{exp}}$ and this reference adiabatic one $\lambda_{\mathrm{ad,CFD}}$ is provided for all mentioned influencing factors on Fig. 12.

The first figure shows the effect of the inlet flow coefficient for four gases, all other parameters remaining constant. It illustrates once more the observation made on Fig. 10, which is the difficulty to remove heat with an increasing flow passing through the stage. This result also confirms that the slope of the work input distribution is different in case of adiabatic or diabatic compression. Moreover, this slope varies with the heat transfer rate as illustrated by changing the gas properties. Another influencing factor is the tip Mach number, whose effect is depicted on Fig. 12(b) for the same gases. As previously noted on Fig. 10, the heat transfer effect on the diabatic work input and efficiency decreases with the tip Mach number. In addition, this figure shows that for all gases this trend diminishes as the tip Mach number increases. Figure 12(c) illustrates the effect of varying the gas properties on the measured work input at three tip Mach number and for a flow impinging the different blade rows at a roughly constant flow angle. Even if to conserve similitude, only about half the mass of gas flows through the stage per unit of time when comparing helium to neon operation, the specific heat capacity is five times higher than the one of neon. This implies that twice more cooling power is required to reduce the temperature by a same amount when operating with helium in comparison to neon. In addition, the characteristic Reynolds number is 45% lower than the one of neon at a same boundary and operating condition leading to a lower heat transfer coefficient for helium operation. This explains the differences observe on Fig. 12(c) between adiabatic and diabatic work input for the various considered gases. As previously illustrated on Fig. 11, the coolant temperature also plays a major role on the diabatic work input and it is further emphasised on Fig. 12(d). Hence, as the coolant temperature increases the diabatic work input increases until the coolant temperature passes above the stage outlet temperature and the heat sink becomes a heat source. The same trend is observed for various gases but at a different rate. The last influencing factor is the inlet temperature. The effect of this parameter at a specific operating point is twofold: it influences the impeller outlet temperature leading to a different heat transfer and changes the heat transfer conducted out of the housing inlet surface and inner walls upstream of the rotor. Thus, increasing the inlet temperature

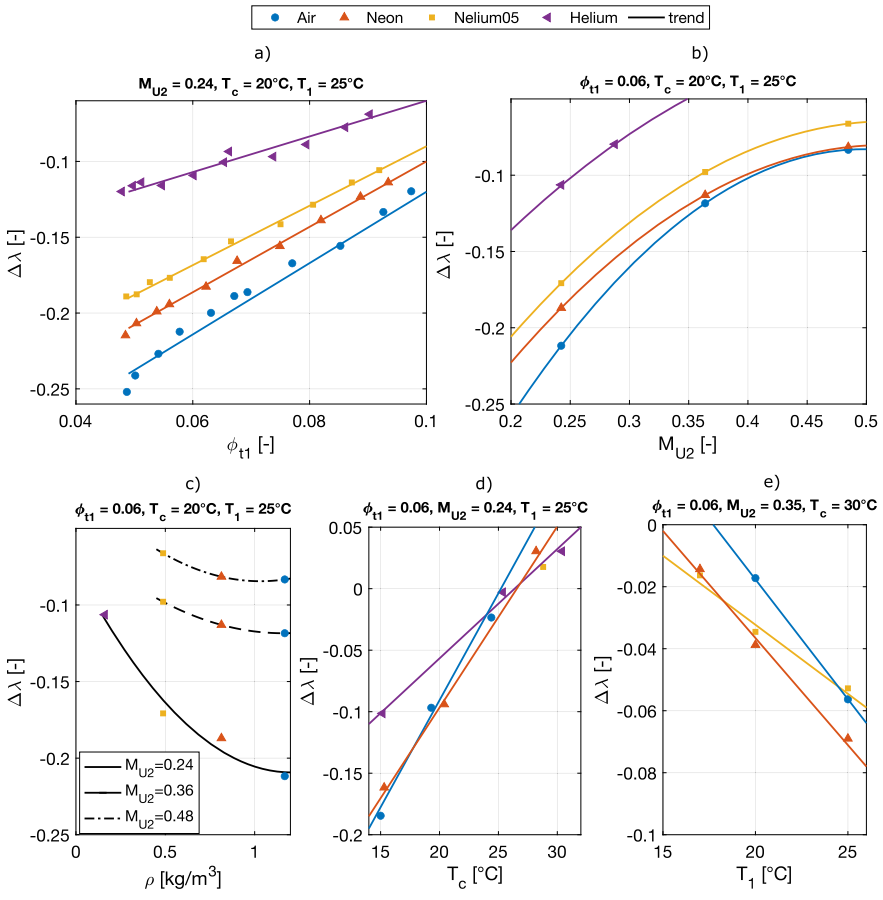

Figure 12 Effect of (**a**) inlet flow coefficient, (**b**) tip Mach number, (**c**) gas properties, (**d**) chiller set temperature and (**e**) inlet stage temperature on the difference between diabatic and adiabatic work input

for all gases increases the heat transfer rate in absolute value leading to a larger difference between adiabatic and diabatic work input.

7 Conclusion

In this paper, a turbocompressor test facility commissioned at the University of Stuttgart and designed to operate for a wide range of low molecular weight gases was first presented together with the geometry of a newly installed compressor stage. Experimental performance was then validated against numerical adiabatic simulation and showed a good agreement for the stage pressure rise. Furthermore, results of diabatic simulations have been presented and confirmed that most discrepancies between measured and numerical adiabatic efficiency can be attributed to a heat transfer occurring with the operating gas due to the presence of a coolant inside the motor housing. A good overall prediction of the heat transfer was obtained with CHT simulation. Finally, the effect of suspected influencing factors on the heat transfer rate were investigated and the impact on stage performance parameters quantified. By combining these results to additional measurement campaign with complementary compressor geometries and building on the results presented here, future research will aim at deriving a unified model to retrieve the adiabatic efficiency from measurements of diabatic performance. Such a model would be valuable in various

applications including the field of turbocharger, the transportation of light gases such as hydrogen or cryogenic applications as for the FCC at CERN. Results presented above and the experimental validation of the stage performance confirm the feasibility of using such a turbocompressor stage to contribute towards an efficient FCC cryogenic pre-cooling cycle.

Acknowledgements
The author would like to thank the ITSM for providing the computing tools and the Marie Skodolwska-Curie Action (MSCA) together with MAN Energy Solutions Zurich AG for their financial support, which made this work possible.

Funding
The presented research was coordinated by the EASITrain project.

EASITrain - European Advanced Superconductivity Innovation and Training. This Marie Sklodowska - Curie Action (MSCA) Innovative Training Networks (ITN) has received funding from the European Union's H2020 Framework Programme under Grant Agreement no. 764879. Open Access funding enabled and organized by Projekt DEAL.

Abbreviations
CHT, Conjugate Heat Transfer; IGV, Inlet Guide Vanes; DAS, Data Acquisition System; PLC, Programmable Logic Controller; CFD, Computed Fluid Dynamics; HMI, Human Machine Interface; RTD, Resistance Temperature Detector.

Availability of data and materials
The data sets used and/or analysed during the current study are available from the corresponding author on reasonable request.

Declarations

Ethics approval and consent to participate
Not applicable.

Consent for publication
All authors agree to the publication of the article.

Competing interests
The authors declare that they have no competing interests.

Authors' contributions
MP designed the experimental setup, conducted the performance measurement as well as the numerical evaluation, analysed the data and wrote the manuscript. DV supervised the research and approved the final manuscript.

Publisher's Note

Received: 29 March 2022 Accepted: 9 June 2022 Published online: 21 June 2022

References

1. Abada A et al. Fcc-hh: the hadron collider. Eur Phys J Spec Top. 2019;228(4):755–1107.
2. Petterson T, Lefèvre P. The large hadron collider, conceptual design. Technical Report 119-135. CERN Geneva; 1995
3. Aungier RH. Centrifugal compressors - a strategy for aerodynamic design and analysis. New York: ASME; 2000.
4. Lüdtke KH. Process centrifugal compressors. Berlin: Springer; 2004.
5. Sirakov B, Casey M. Evaluation of heat transfer effects on turbocharger performance. J Turbomach. 2013;**135**(2)
6. Baines N, Wygant KD, Dris A. The analysis of heat transfer in automotive turbochargers. J Eng Gas Turbines Power. 2010;**132**(4)
7. Podeur M, Vogt DM. Experimental and numerical similitude study using a novel turbocompressor test facility operating with helium-neon gas mixtures. In: Proceedings of ASME turbo expo 2021. ASME; 2021.
8. NUMECA: FINE/Turbo V8. 7, User Manual. NUMECA International, Brussels (2009). NUMECA International
9. ANSYS: ANSYS CFX-Solver Theory Guide, Release 15.0. ANSYS, Inc., Canonsburg (2013). ANSYS, Inc.
10. Lemmon EW, Bell IH, Huber ML, McLinden MO. NIST Standard Reference Database 23: Reference Fluid Thermodynamic and Transport Properties-REFPROP, Version 10.0. National Institute of Standards and Technology. 2018. National Institute of Standards and Technology
11. Casey MV, Robinson CJ. A unified correction method for reynolds number, size, and roughness effects on the performance of compressors. IMECHE J Power and Energy. 2011;**225**(7)